Radio Science

RESEARCH ARTICLE
10.1029/2019RS006939

Key Points:
- It is possible to use a patch antenna to produce radiation that cancels the scattering of a radar signal from an arbitrary object, thus reducing its radar cross section (RCS)
- Microstrip antennas with a bandwidth larger than the bandwidth of the radar signal are used for this purpose; an electromagnetic sensor is employed along with an amplifier and phase shifter to produce the patch radiation
- This method works best for RCS reduction against a known monostatic radar

Correspondence to:
S. Sengupta,
sohiniseng@gmail.com

Citation:
Sengupta, S., Council, H., Jackson, D. R., & Onofrei, D. (2020). Active radar cross section reduction of an object using microstrip antennas. *Radio Science*, *55*, e2019RS006939. https://doi.org/10.1029/2019RS006939

Received 25 AUG 2019
Accepted 2 FEB 2020
Accepted article online 5 FEB 2020

Active Radar Cross Section Reduction of an Object Using Microstrip Antennas

Sohini Sengupta[1], Henry Council[2], David R. Jackson[2], and Daniel Onofrei[1]

[1]Department of Mathematics, University of Houston, Houston, TX, USA, [2]Department of Electrical and Computer Engineering, University of Houston, Houston, TX, USA

Abstract The research performed in this paper suggests that the radar cross section of an arbitrarily shaped object can be reduced by canceling the scattering from the object with the radiation from an antenna (implemented here as a microstrip antenna) placed on the surface of the object. Assuming that the direction of arrival of the incident signal is known, the radiation from the defending antenna can be adjusted in real-time to cancel the scattering from the object in order to produce a negligible total field at the distant receiver so that the object becomes invisible to a monostatic radar working in a given known frequency band. This is implemented using an analog sensor on the object to measure the time domain field on the object, which is then connected to the antenna through an amplifier and phase shifter to control the radiation from the patch antenna. The system is implemented in real time and does not require any digitization or signal processing. The radar cross section reduction can thus be achieved with a wide variety of incident signals in the prescribed frequency band.

1. Introduction

The scattering from certain objects such as wind farms, towers, and other objects or installations often needs to be reduced to make them invisible to radar, that is, to reduce the radar cross section (RCS) of the objects. There are several passive approaches for implementing RCS reduction, such as coating the object with Radar Absorbing Materials, covering the object with a metamaterial, altering the shape of the object to reduce scattering in a certain direction, etc. These techniques are most effective at higher frequencies, where the object is large relative to a wavelength. Reducing the RCS at low frequencies is a challenging problem for many scattering objects. The approach adopted here is one way to address this issue.

There is a comprehensive discussion of the different RCS reduction techniques, both passive and active, in Ufimtsev (1996). There have also been a number of studies on the reduction of RCS using metasurfaces with both passive loading (Li et al., 2017; Su, Kong, Li, Yin, et al., 2017; Su, Kong, Li, Yuan, et al., 2017; Zhang et al., 2017) as well as active loading (Kord et al., 2016; Li et al., 2016; Sui et al., 2017). In Ghayekhloo et al. (2017) the absorption of X-band radar signals using a thin layer of collisional plasma is proposed and is analyzed as well as experimentally verified for normal or oblique incidence. Some of the RCS reduction techniques use active impedance surfaces such as a phase switched surface to reduce the RCS (Tennant & Chambers, 2005). An active cancellation scheme against synthetic aperture radar that is achieved in three stages using frequency and delay modulation is presented in Xu et al. (2015).

These methods are typically narrowband, and therefore, several of the more recent works are focused on ensuring wideband RCS reduction using active and passive loading as proposed in Chen et al. (2013), where metasurfaces are loaded with active circuitry using varactor diodes and non-Foster circuit elements to get a wider bandwidth of RCS reduction using real-time tunability. This method has been shown to work with simulation and experimental results in Soric et al. (2013). Some more cases of wideband RCS reduction have been realized using optimized pixelated metasurfaces in Haji-Ahmadi et al. (2017), loaded chessboard-like metamaterial surfaces in Zheng et al. (2017), and metamaterials integrated with a dielectric absorber in Baskey et al. (2017).

Another way to reduce the RCS of an object is by producing an opposing radiation from one or more antennas placed on the object that cancels the scattering from the object, thus rendering the object invisible to the radar. A number of theoretical works have demonstrated this principle. Miller's work on active cloaking strategy in Miller (2006) suggested numerically that active boundaries could be used for RCS reduction, and the series of papers by Milton, Onofrei, and Guevara-Vasquez have theoretically and numerically

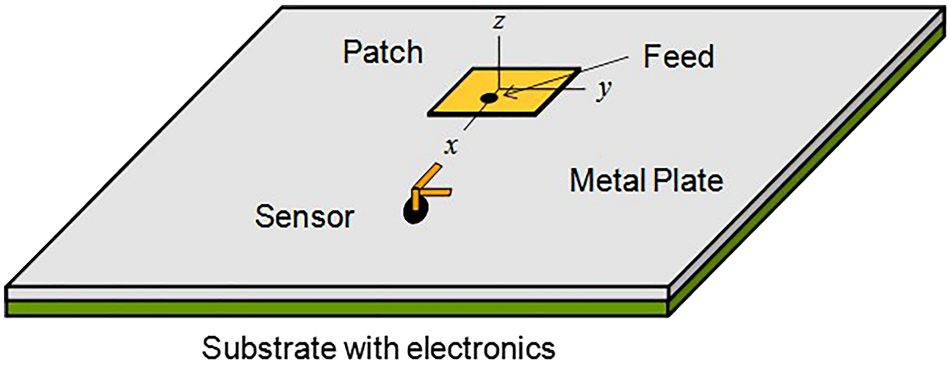

Figure 1. The layout of the patch antenna and sensor on an object, with the object taken here to be a metal (copper) plate for simplicity.

proved in Guevara Vasquez, Milton, Onofrei, and Seppecher (2011), Guevara Vasquez, Milton, and Onofrei (2011), Guevara Vasquez et al. (2009a, 2012, 2009b) the possibility for field manipulation to cancel the scattering from an object using radiating elements. A numerical treatment using boundary element strategies for the same problem was proposed in Zheng et al. (2010). In these works, cancellation of both electrostatic fields has been shown, as well as time-varying scalar fields in two and three dimensions by using integral representation theorems. More recently, in Onofrei (2012, 2014), Onofrei proposed a unified integral equation method for the construction of a class of approximate solutions for the problem of scalar field manipulation using scalar sources. A sensitivity study for this design in the context of scalar field scattering cancellation was proposed in Norris et al. (2012) and Hubenthal and Onofrei (2016). The extension of the scalar results to electromagnetic guided waves was studied by Albanese and Onofrei *(2017)*. The works in Selvanayagam and Eleftheriades (2012, 2013) make use of the equivalence principle, and show how a dipole array can cancel the known electromagnetic field scattered by a cylinder. These numerical approaches based on active cloaking have been supported by experimental results in Ma et al. (2013) for the quasistatic regime, and in Du et al. (2012) for the finite frequency regime.

Another interesting alternative approach is proposed in Sheng and Yuanming (2012, 2014a, 2014b) in which a strategy of active scattering cancellation is proposed, which takes measurements of the incident field in real time and implements scattering cancellation based on a precomputed accurate dictionary of broadband omnidirectional scattering patterns. The scheme is based on a digital circuit that actively matches the measured interrogating field to the dictionary of scattering patterns in real time and signals the sources to produce radiation that cancels the scattered signal. However, this method would entail delays in reacting to the interrogating signal in the circuits and digital processing, which might prove to be a disadvantage. Some of the methods described have been used to reduce RCS of wind turbines: Brock and et al. (2012), Naqvi and Ling (2013), Palmer and Torres (2011), Pinto et al. (2010), and Raza and Fickenscher (2013). A comprehensive discussion of existing RCS reduction techniques for phased arrays is provided in H. Singh and Jha (2015), where the authors mainly focus on the RCS due to the coupling between the array and an incident field (the so-called antenna mode scattering).

In this work we propose a general real-time RCS reduction scheme to reduce the transient scattered signal from an object using a sensor on the object and a radiating antenna, taken here to be a microstrip antenna (Sengupta et al., 2017). Our scheme is designed to work for a prescribed central frequency and the interrogating radar is assumed here to be monostatic with the radar transmitter/receiver in the far-field region of the object. We also assume that the direction of arrival of the incident signal can be a priori determined. The scattered signal from the object is canceled by producing an opposing radiated field using a microstrip patch antenna placed on the object as shown in Figure 1, where the object is taken as a metal plate for simplicity. The incident field near the antenna is measured using an analog sensor (details on the sensor are given later) and this information is used to control the radiation from the antenna, using an amplifier and a phase shifter, in order to produce the desired radiation that will cancel the scattered field produced by the object.

The scheme proposed here is somewhat similar in concept to that introduced in Semenikhin and Chernokolpakov (2017, 2019), where a scattering cancellation scheme was also introduced. However, in

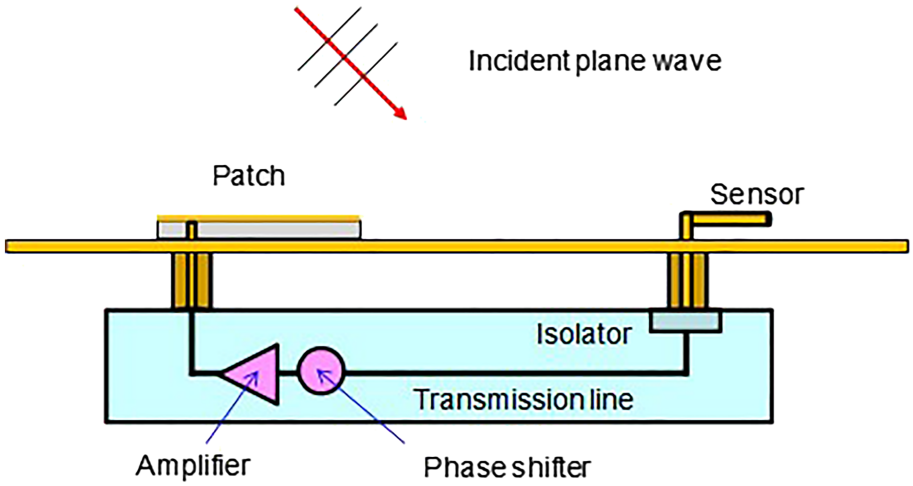

Figure 2. Geometry of a patch on an object (metal plate), connected by a transmission line to a sensor via an isolator, amplifier, and phase shifter.

those references there was no active scattering cancellation using a sensor and amplifier/phase shifter; a hypothetical amplifier and phase shift were imposed at the radiating antenna element, which were calculated ahead of time. The proposed system builds on this by having an active scattering cancellation scheme using active electronics.

We also mention that the present study builds up on previous work developed in Albanese and Onofrei (2016), where the authors explored the possibility of active scattering cancellation of fields scattered from a plate by using a feedback loop formed by a dipole antenna and a sensor placed in front of the plate.

The simple layout shown in Figure 1 has been analyzed to examine the possibility of implementing RCS reduction for a practical scenario using practical radar signals such as rectangular pulse modulated carrier, a Gaussian pulse modulated carrier, and a chirped pulse. This gives insight into the effectiveness and the limitations of the method, possible areas of improvement, and ways to adapt this method to more complicated structures. Although a simple metal plate is used as the scattering object, the methodology applies equally well to any scattering object of similar size in terms of a wavelength.

2. RCS Reduction Methodology

The RCS reduction methodology uses a radiating microstrip patch antenna that is mounted on a scattering object, whose RCS is to be reduced. Although the theoretical study we present below is valid for an arbitrary scattering object, our numerical simulation will consider the simpler situation depicted in Figure 2, where a rectangular perfect electric conductor plate is used as the scattering object, fitted with a patch antenna on the top surface. An incident time-varying plane wave signal from a radar is assumed to be incident from above the structure. The job of the patch antenna is to produce an opposing radiation to cancel the natural scattering from the object (the scattered field that would be created by the plate without the patch present). The radiation from the patch is controlled by using an analog sensor to detect the field at the given sensor location, with the output of the sensor amplified and phase shifted (by a delay line) and then fed into the patch to produce the radiation from the patch. This simple setup is shown in Figure 2. A high-impedance isolator is used to avoid loading down the sensor. All of the electronics is contained behind the plate, to avoid radiation from the electronics in the direction of the radar. If the object were a three-dimensional one, the electronics could be contained inside the object, or within a cavity that is placed inside the object.

Because a single patch and sensor is assumed, this scheme can work only for a fixed angle of incidence of the radar signal. (It may be possible to extend the method to cover multiple angles of incidence together with more general radars (e.g., bistatic or multistatic) by using multiple patches and sensors, but that is not considered here.) Also, a fixed known polarization of the incident field is assumed as well. It may be possible to extend the technique to canceling the scattering due to an arbitrarily polarized incident signal using two patches and two sensors (or a dual-polarized patch), but this is not explored here.

If the incoming plane wave was a pure sinusoidally varying (time-harmonic) signal at radian frequency ω_0, the phase and amplitude of the voltage at the patch feed could be selected to ensure that the patch radiation exactly cancels the natural scattering of the object. That is, the amplifier and phase shifter could be selected to produce a feed voltage at the patch so that the patch radiation has the necessary amplitude and phase to cancel the natural scattering from the object. However, in a practical radar system, the incident plane wave will be a time-varying signal. If the time variation is completely arbitrary, then canceling the scattering from the object would be very difficult. However, it is assumed here that the incoming plane wave consists of a sinusoidal carrier at radian frequency ω_0 that is modulated in some way, for example, by a direct amplitude modulation of the pulse envelope or by varying the frequency of the carrier with time (a chirped pulse). If the incident signal has a small or perhaps moderate bandwidth, the cancellation scheme becomes feasible. That is, even though the cancellation can only be perfect at one frequency, the cancellation may remain fairly good over a bandwidth of frequencies if the bandwidth of the signal is not too large. The amplifier and phase shifter are selected so that the patch is fed with the necessary voltage amplitude and phase required to cancel the natural scattering of the object exactly at the carrier frequency, which is chosen as the resonance frequency of the patch. The smaller the bandwidth of the incident signal is, the more the RCS will then be reduced across the bandwidth of the signal, and hence the smaller will be the amplitude of the time-varying scattered field produced from the complete system (the object together with the radiating patch).

Because of the transmission line that connects the electronic components together, and because of the components themselves, there will be a time delay in the system in going from the sensor to the radiating patch, and the effects of this delay are important and will be examined later. The time delay means physically that we cannot instantaneously cancel the scattered field that is created at the moment the incident signal first impinges on the scattering object. Therefore, the scattering cancellation can never be perfect. It is desired to make the transmission line as short as possible, no longer than is absolutely necessary to connect the components together.

These two points of view are commensurate, since a longer time delay in the system means that there is a more rapid change in the phase of the voltage at the patch feed as the frequency changes, lowering the bandwidth over which the scattering cancellation is effective.

3. Analysis and Design of System

3.1. Definition and Calculation of Coefficient Functions

It is assumed here that there is a constant of proportionality in the frequency domain between the open-circuit output voltage of the sensor (V_S) and the open-circuit output voltage of the amplifier (V_A) that is fed into the patch. This constant of proportionality, denoted as $A(\omega)$, is chosen so that the patch radiation cancels the scattering from the object for a particular frequency ω_0. This constant of proportionality $A(\omega)$ is provided by the amplifier, phase shifter and transmission line assembly in Figure 2. The amplifier is assumed to have an output impedance of Z_{out}. The voltage at the feed port of the patch due to the amplifier is then given by

$$V_p^A(\omega) = V_A(\omega)\left(\frac{Z_{in}(\omega)}{Z_{out} + Z_{in}(\omega)}\right), \tag{1}$$

where the input impedance of the patch seen at the feed port as a function of frequency is denoted as $Z_{in}(\omega)$. The incident wave that impinges on the system will also set up a voltage at the feed of the patch. This is the voltage at the feed port if the amplifier voltage was turned off, so that the patch is terminated with a load impedance of Z_{out}. The feed port voltage with the amplifier turned off is

$$V_p^{inc}(\omega) = V_{oc}^{inc}(\omega)\left(\frac{Z_{out}}{Z_{out} + Z_{in}(\omega)}\right), \tag{2}$$

where $V_{oc}^{inc}(\omega)$ is the open-circuit voltage at the feed port when the plane wave is incident and the patch is left open circuited at the feed port. We then have the total patch feed port voltage as

$$V_p(\omega) = V_A(\omega)\left(\frac{Z_{in}(\omega)}{Z_{out} + Z_{in}(\omega)}\right) + V_{oc}^{inc}(\omega)\left(\frac{Z_{out}}{Z_{out} + Z_{in}(\omega)}\right). \tag{3}$$

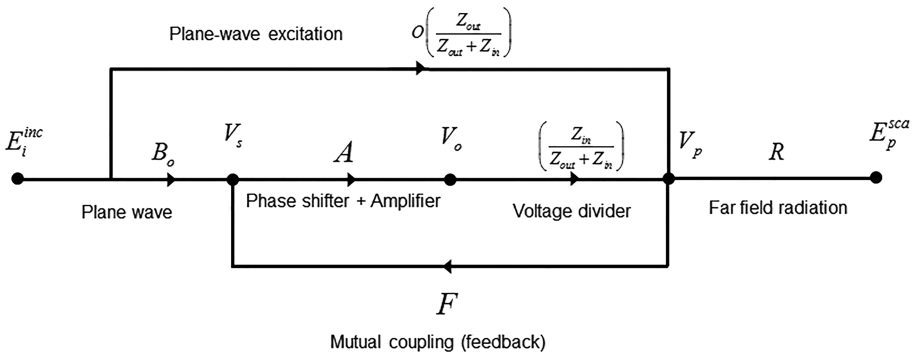

Figure 3. Signal-flow graph of the amplifier and phase shifter system connecting the sensor to the patch.

The electronic system connecting the sensor to the patch is shown as a signal-flow graph in Figure 3. The plane wave excitation of the patch as well as the presence of the feedback loop due to the mutual coupling between the patch and the sensor, which introduces a feedback coefficient F, is shown in Figure 3.

In the frequency domain, the field component E_p^{sca} giving the scattered electric field in the p direction (i.e., the polarization of the scattered field) at a location (r, θ, ϕ) from the system has the form

$$E_p^{sca}(\omega,\theta,\phi) = \left(\frac{e^{-jk_0 r}}{r}\right)\left[E_i^{inc}S[\omega] + R[\omega]V_p[\omega]\right]. \tag{4}$$

The coefficient $S(\omega)$ denotes the scattered field from the object with the patch present but short-circuited at the feed port, when the system is illuminated by a unit-amplitude incident plane wave with component E_i^{inc} (i.e., polarized in the i direction) at frequency ω. (A short-circuited patch radiates very little at the original resonance frequency, so it may be assumed that this coefficient approximately denotes the scattering from the object when the patch is absent.) The term V_p is the voltage at the feed port. The coefficient $R(\omega)$ gives the radiated field by the patch on the object, when fed with a unit-amplitude voltage at the feed port (i.e., $V_p = 1$ V) (Note that by definition it also includes any coupling between the patch and the plate when radiating). Accounting for the amplifier + phase shifter + transmission line circuit, we have that

$$V_A(\omega) = A(\omega)V_s(\omega), \tag{5}$$

where $A(\omega)$ denotes the complex gain of the amplifier, phase shifter, and the transmission line network, and hence,

$$E_p^{sca} = \left[E_i^{inc}S[\omega] + R[\omega]V_{oc}^{inc}[\omega]\left[\frac{Z_{out}}{Z_{out}+Z_{in}[\omega]}\right] + R[\omega]A[\omega]V_s[\omega]\left[\frac{Z_{in}[\omega]}{Z_{out}+Z_{in}[\omega]}\right]\right]\left(\frac{e^{-jk_0 r}}{r}\right). \tag{6}$$

The sensor voltage is proportional to the amplitude of the incoming wave in the frequency domain, where the constant of proportionality $B(\omega)$ also includes the mutual coupling between the patch and the sensor, and hence the feedback term F in Figure 3, so that

$$V_s(\omega) = B(\omega)E_i^{inc}(\omega). \tag{7}$$

The coefficient $B(\omega)$ can be related to the corresponding coefficient $B_0(\omega)$, which gives the open-circuit sensor voltage due to the plane wave in the absence of the patch. To see this relationship, we can use

$$V_s(\omega) = B_0(\omega)E_i^{inc}(\omega) + V_p(\omega)F(\omega), \tag{8}$$

where the feedback coefficient $F(\omega)$ gives the open-circuit sensor voltage picked up due to a one volt patch excitation at the feed port. The feedback coefficient $F(\omega)$ arises from the mutual coupling between the patch

and the sensor, and physically gives the sensor output that is due to radiation from the patch antenna. We also have, from equations (3) and (5) (suppressing the frequency in the notation)

$$V_p = V_s A\left(\frac{Z_{in}}{Z_{in}+Z_{out}}\right) + E_i^{inc} O\left(\frac{Z_{out}}{Z_{out}+Z_{in}}\right), \tag{9}$$

where the $O(\omega)$ coefficient is defined as the open-circuited feed port voltage due to a unit-amplitude incident plane wave, where $E_i^{inc} = 1$ V/m. Combining equations (8) and (9) yields

$$V_s = B_0 E_i^{inc} + F\left(V_s A\left(\frac{Z_{in}}{Z_{in}+Z_{out}}\right) + E_i^{inc} O\left(\frac{Z_{out}}{Z_{out}+Z_{in}}\right)\right), \tag{10}$$

or

$$V_s\left[1 - AF\left(\frac{Z_{in}}{Z_{in}+Z_{out}}\right)\right] = E_i^{inc}\left[B_0 + OF\left(\frac{Z_{out}}{Z_{in}+Z_{out}}\right)\right]. \tag{11}$$

Substituting from equation (7) into (11), we have (putting back frequency in the notation)

$$B(\omega) = \frac{B_0(\omega) + O(\omega)F(\omega)\left(\frac{Z_{out}}{Z_{in}(\omega)+Z_{out}}\right)}{1 - A(\omega)F(\omega)\left(\frac{Z_{in}(\omega)}{Z_{in}(\omega)+Z_{out}}\right)}. \tag{12}$$

If the mutual coupling between the patch and the sensor (denoted by the $F(\omega)$ coefficient) is small, then the $B(\omega)$ coefficient relates the sensor voltage directly to the incident field amplitude, and is thus a slowly varying function of frequency. If the mutual coupling is small and the sensor is also small, then the $B(\omega)$ coefficient will not be a function of frequency, but will only involve the effective length of the sensor probe.

Combining equations (6) and (7), the scattered field in the frequency domain can be written, incorporating the $B(\omega)$ coefficient. This yields the result

$$E_p^{sca} = E_i^{inc}\left[S(\omega) + R(\omega)O(\omega)\left(\frac{Z_{out}}{Z_{out}+Z_{in}(\omega)}\right) + R(\omega)A(\omega)B(\omega)\left(\frac{Z_{in}(\omega)}{Z_{out}+Z_{in}(\omega)}\right)\right]\left(\frac{e^{-jk_0 r}}{r}\right). \tag{13}$$

For canceling the scattered field due to an incident signal polarized in the i direction, we would normally choose $p = i$; that is, the polarization direction of the patch radiation (denoted by p) that we are interested in would normally be chosen to be the same as the polarization direction of the incident radar signal i. For example, if the incident signal is polarized in the θ direction, we would normally choose to reduce the θ component of the scattered field.

In order to cancel the scattered field by the patch radiation, we assume that the constant $A(\omega_0)$ has been chosen (by choosing the gain of the amplifier and the phase difference produced by the phase shifter) to achieve perfect cancellation of the scattered field at the resonance frequency of the patch ω_0, which is also chosen to be the same as the carrier frequency of the incoming signal. Therefore, $E_p^{sca}(\omega_0, \theta, \phi) = 0$. This results in

$$S(\omega_0) + R(\omega_0)O(\omega_0)\left(\frac{Z_{out}}{Z_{out}+Z_{in}(\omega_0)}\right) + R(\omega_0)A(\omega_0)B(\omega_0)\left(\frac{Z_{in}(\omega_0)}{Z_{out}+Z_{in}(\omega_0)}\right) = 0. \tag{14}$$

Therefore,

$$A(\omega_0) = -\frac{S(\omega_0) + R(\omega_0)O(\omega_0)\left(\frac{Z_{out}}{Z_{out}+Z_{in}(\omega_0)}\right)}{R(\omega_0)B(\omega_0)\left(\frac{Z_{in}(\omega_0)}{Z_{out}+Z_{in}(\omega_0)}\right)}. \tag{15}$$

Equation (15) is the basic design equation that indicates how to choose the amplifier gain and the phase of the phase shifter (based on the magnitude and phase of $A(\omega_0)$). The $A(\omega)$ coefficient accounts for the delay in the system due to the transmission line that connects the components together, as well as any other delays in

the electronics. We assume here that the delay is represented by a length L of transmission having an effective relative permittivity ε_r^{eff}. We then have

$$A(\omega) = A(\omega_0)e^{-j(k_0(\omega)-k_0(\omega_0))\sqrt{\varepsilon_r^{eff}}L}, \tag{16}$$

The open-circuit voltage coefficient $O(\omega)$ can be related to the radiation coefficient $R(\omega)$ through reciprocity (Harrington, 2001; Balanis, 2012). To do this, consider a unit-amplitude "testing" dipole "a" in the far field at (r, θ, ϕ), in the direction of $\underline{\hat{p}}$, which is the direction in which the incident plane wave is polarized (a direction perpendicular to $\underline{\hat{r}}$). A "testing" current "b" is introduced, consisting of a 1A filament of current running from the inner conductor to the outer conductor of the feeding coax at the base of the patch antenna. The base of the antenna is left open circuited. We then have

$$\langle a, b\rangle = E_0\, O(\omega), \tag{17}$$

where

$$E_0 \equiv \left(\frac{-j\omega\mu_0}{4\pi r}\right) e^{-jk_0 r}. \tag{18}$$

We also have

$$\langle b, a\rangle = -Z_{in}(\omega)R(\omega)\left(\frac{e^{-jk_0 r}}{r}\right). \tag{19}$$

From reciprocity, $\langle b,a\rangle = \langle a,b\rangle$. Hence, we have

$$O(\omega) = \frac{-Z_{in}(\omega)R(\omega)\left(\frac{e^{-jk_0 r}}{r}\right)}{E_0} = -Z_{in}(\omega)R(\omega)\left(\frac{4\pi}{-j\omega\mu_0}\right). \tag{20}$$

3.2. Calculation of the Scattered Field

The scattered signal in the time domain can be found from the Fourier transform of the scattered signal in the frequency domain. Suppressing the $\exp(-jk_0 r/r)$ term in equation (13), and normalizing the result by dividing by $S(\omega_0)$, the normalized scattered field is given by

$$E_p^{Nsca}(t) = \frac{1}{2\pi}\int_{-\infty}^{\infty} \widetilde{E}_p^{Nsca}(\omega)e^{j\omega t}\, d\omega = \frac{1}{\pi}\mathrm{Re}\int_0^{\infty} \widetilde{E}_p^{Nsca}(\omega)e^{j\omega t}\, d\omega, \tag{21}$$

where the tilde denotes Fourier transform and the superscript N denotes "normalized" by suppressing the $\exp(-jk_0 r/r)$ term and dividing by $S(\omega_0)$. In the frequency (phasor) domain, the ratio of the scattered field to the incident field at any frequency ω is the same as the ratio of the Fourier transform of the scattered signal to the transform of the incident signal at the same frequency ω. Therefore, we have

$$\widetilde{E}_p^{Nsca}(\omega) = \widetilde{E}_i^{inc}(\omega)\left[\frac{S(\omega)}{S(\omega_0)} + \frac{R(\omega)}{S(\omega_0)}O(\omega)\left(\frac{Z_{out}}{Z_{out}+Z_{in}(\omega)}\right) + \frac{R(\omega)}{S(\omega_0)}A(\omega)B(\omega)\left(\frac{Z_{in}(\omega)}{Z_{out}+Z_{in}(\omega)}\right)\right]. \tag{22}$$

4. CAD Formula for Scattered Field

If we assume that the $S(\omega)$ and $B(\omega)$ coefficients are fairly slowly varying functions of frequency (compared with the patch response) and can be assumed to be constants, and we assume equation (16) holds, then the normalized scattered electric field is, after some simplification,

$$\widetilde{E}_p^{Nsca}(\omega) \approx \widetilde{E}_i^{inc}(\omega)\left[1 - H[\omega]e^{-j[\omega-\omega_0]\sqrt{\varepsilon_r^{eff}}\frac{L}{c}} - G[\omega]\right], \tag{23}$$

where

$$H(\omega) \equiv \left\{1 - \frac{R^2(\omega_0)Z_{in}(\omega_0)\left(\frac{j4\pi}{\omega_0\mu_0}\right)}{S(\omega_0)}\left(\frac{Z_{out}}{Z_{out}+Z_{in}(\omega_0)}\right)\right\}\left(\frac{\frac{Z_{in}(\omega)}{Z_{out}+Z_{in}(\omega)}}{\frac{Z_{in}(\omega_0)}{Z_{out}+Z_{in}(\omega_0)}}\right)\left(\frac{R(\omega)}{R(\omega_0)}\right), \tag{24}$$

and

$$G(\omega)\equiv\frac{R^2(\omega)Z_{in}(\omega)\left(\frac{j4\pi}{\omega\mu_0}\right)}{S(\omega_0)}\left(\frac{Z_{out}}{Z_{out}+Z_{in}(\omega)}\right). \tag{25}$$

Using a simple CAD model of a microstrip antenna, the input impedance of a patch antenna is (Jackson, 2019)

$$Z_{in}(\omega)=\frac{R_0}{1+j2Q\left(\frac{\omega}{\omega_0}-1\right)}+jX_p(\omega). \tag{26}$$

Here Q is the quality factor of the patch, which is inversely proportional to the bandwidth of the patch (the relative impedance bandwidth BW is given as $\mathrm{BW}=1/(\sqrt{2}Q)$ (Jackson, 2019)), and X_p is the probe reactance. We further assume a fixed probe inductance, so that the probe reactance varies linearly with frequency. Cavity model theory (Jackson, 2019) (along with the linear behavior of the radiation from a magnetic dipole) predicts that

$$R(\omega)\ \propto\ \omega A_{10}(\omega)\left(\frac{1}{Z_{in}(\omega)}\right), \tag{27}$$

where $A_{10}(\omega)$ is the amplitude of the vertical electric field of the (1,0) patch mode inside the cavity due to a 1A feed current. This is then proportional to the input impedance of the (1,0) mode, so that

$$R(\omega)\ \propto\ \omega\left(\frac{Z_{in}(\omega)-jX_p(\omega)}{Z_{in}\omega}\right), \tag{28}$$

or

$$R(\omega)\ \propto\ \omega\left(1-j\frac{X_{p0}\left(\frac{\omega}{\omega_0}\right)}{Z_{in}(\omega)}\right), \tag{29}$$

where X_{p0} denotes the reactance of the probe at the resonant frequency ω_0. We then have in equation (24) that

$$\frac{R(\omega)}{R(\omega_0)}=\frac{\omega}{\omega_0}\left(\frac{1-j\frac{X_{p0}\left(\frac{\omega}{\omega_0}\right)}{Z_{in}(\omega)}}{1-j\frac{X_{p0}}{Z_{in}(\omega_0)}}\right). \tag{30}$$

Equation (23), together with equations (24) through (30), gives the final approximate CAD formula for the Fourier transform of the time domain scattered field (time domain signal) produced by the scattering cancellation scheme shown in Figure 2. Equation (21) is then used to give the time domain signal. If the amplifier is ideal with a zero output impedance, then equation (23) simplifies greatly to

$$\widetilde{E}_p^{Nsca}(\omega)\ \approx\ \widetilde{E}_i^{inc}(\omega)\left[1-\frac{\omega}{\omega_0}\left[\frac{1-j\frac{X_{p0}\left[\frac{\omega}{\omega_0}\right]}{Z_{in}[\omega]}}{1-j\frac{X_{p0}}{Z_{in}[\omega_0]}}\right]e^{-j[\omega-\omega_0]\sqrt{\varepsilon_r^{eff}}\frac{L}{c}}\right]. \tag{31}$$

This result makes it clear that the main characteristics that determine the scattering cancellation behavior are the impedance properties of the patch (i.e., the bandwidth of the patch) and the delay in the system.

5. Results

Results are presented for various incident radar signals that are impinging at normal incidence (broadside) onto a perfectly conducting metal plate. A single radiating patch antenna is assumed to be connected to the sensor with an isolator, phase shifter, and amplifier, as shown in Figures 1 and 2. Exact results are obtain

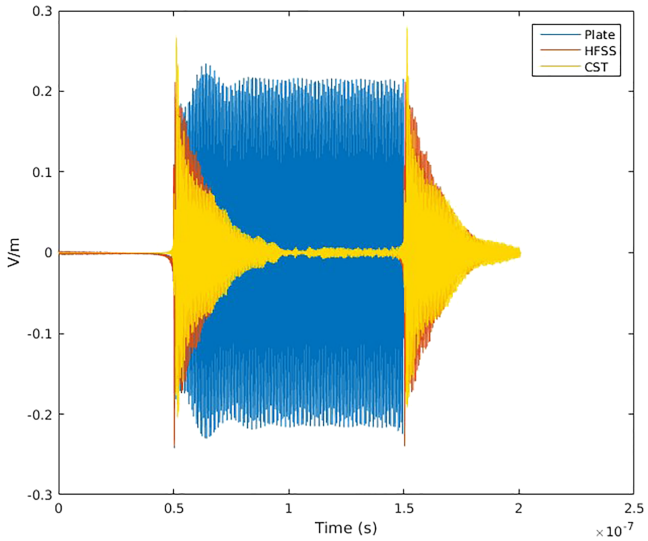

Figure 4. The scattered signal from the rectangular pulse modulated incident signal without scattering cancellation, and the scattered signal with scattering cancellation, from HFSS and CST.

using equation (13) together with equations (15) and (16), while approximate results are obtained using the CAD formula (23) together with equations (24)–(26) and (30). In both cases equation (21) is used to calculate the final time domain scattered signal using the frequency domain data.

The simulations were done in Ansys HFSS and CST microwave studio—two commercially available full-wave simulation software tools. In most of the simulations that were done the system coefficients, including $R(\omega)$, $S(\omega)$, $F(\omega)$, and $B_0(\omega)$, were extracted from HFSS and CST in the frequency domain and then combined using the relations of section 3 to get the scattered radar signal in the time domain for the entire system. A full system transient simulation was also done using the time-domain solver CST. In this simulation a transient plane wave excitation was used to obtain the output voltage of the sensor, and this was fed into an electronic system consisting of a TEM transmission line (to obtain the necessary phase shift at the carrier frequency) and an amplifier (with a constant gain). The electronic system was then fed into the patch antenna, which was also simultaneously excited by the transient plane wave. The scattered signal in the time domain was then calculated.

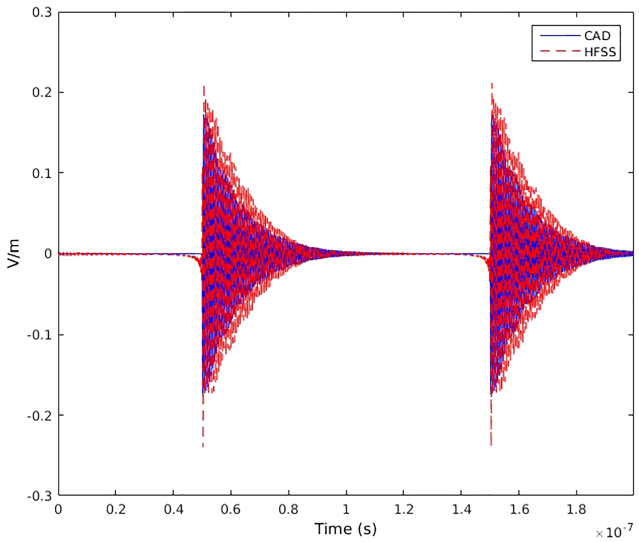

Figure 5. The scattered signal from the rectangular pulse modulated incident signal with scattering cancellation, from HFSS and the CAD formula based on theoretical analysis.

In all of the calculations presented in this paper the regular sensor was placed at a distance of 0.2 m (about one free-space wavelength) from the patch (measured to the closest edge) in the H plane of the patch, where the mutual coupling from the patch was small; hence $F(\omega) \approx 0$ and hence $B(\omega) \approx B_0(\omega)$. The supersensor introduced in section 6 is designed to not be affected by the mutual coupling from the patch, even when it is placed quite close to the patch, and hence in case of the supersensor $F(\omega) \approx 0$ and $B(\omega) \approx B_0(\omega)$ for all separations between the patch and the sensor, including separations as small as 0.25 free-space wavelengths.

In sections 5.1 and 5.2 there is no delay in the system ($L = 0$). In sections 5.3 and 5.4, results are presented for various amounts of delay in order to study the effect of delay in the system.

5.1. Rectangular Pulse Modulated Radar Signal

We take the case of the rectangular perfect electric conductor plate of size 20 cm × 20 cm, that is shielded from detection by a radar signal by a single patch antenna in the center of the plate. The rectangular patch antenna has a length of 6.255 cm and width of 9.383 cm in the x and y directions,

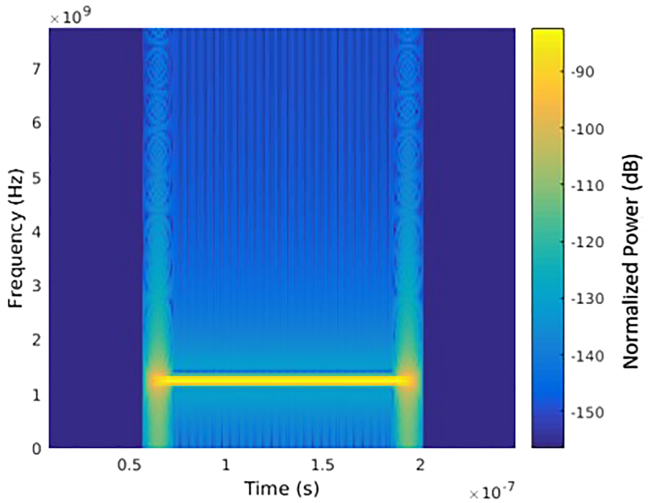

Figure 6. The spectrogram of the incident rectangular pulse modulated signal from the radar.

respectively (x is the resonant dimension), on a substrate of height 1.524 mm and relative permittivity 2.2. The patch has a quality factor of 58.24 at the center frequency of operation of the system, which is 1.575 GHz, and the amplifier and phase shifter circuit is designed to cancel the scattering at broadside for this frequency. The incident and scattered electric field are polarized in the x direction. (This may be thought of as a limiting case of TM_z incidence in the E plane ($\phi = 0$) or TE_z incidence in the H plane ($\phi = \pi/2$), for $\theta = 0$.) The sensor used in the system to measure the incident field is a planar bent-monopole with two perpendicular branches. (More details about the sensor design are given in section 6.) Each branch of the sensor is a strip of length 1 cm and width 0.15 cm, fed by a coaxial probe.

The radar transmitter and receiver are taken to be far away from the plate so as to be in its far-field region. The signal transmitted from the radar is a rectangular pulse modulated signal of carrier frequency 1.575 GHz, and the width of the pulse is 200 ns. The bandwidth of this pulse is approximately 0.3%, since the rectangular envelope contains approximately 315 cycles of the carrier. (The relative bandwidth is roughly the reciprocal of the number of cycles of the carrier contained within the rectangular pulse). Figure 4 shows the signal scattered from the plate without scattering cancellation (blue curve), as well as the normalized scattered signal from the plate with the scattering cancellation (implemented with the patch and sensor on it), computed using both Ansys HFSS and CST Microwave Studio frequency domain solvers (red and yellow curves).

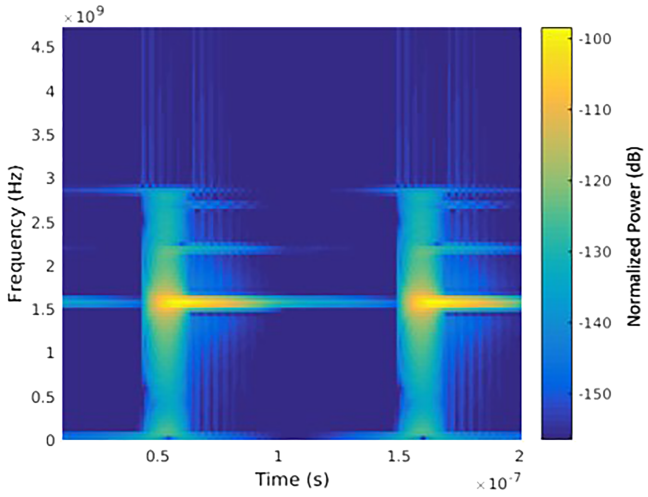

Figure 7. The spectrogram of the signal scattered from the plate with scattering cancellation.

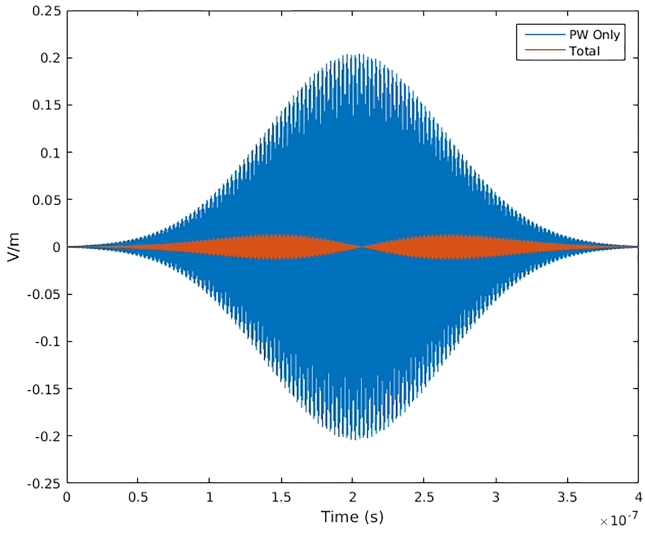

Figure 8. The scattered signal from the Gaussian pulse modulated incident signal without scattering cancellation (blue curve) and also with scattering cancellation (red curve), from HFSS.

The same scattered signal has also been calculated using the approximate CAD formula described in section 4 and is given in Figure 5, along with the result from HFSS. We see that the simple CAD formula predicts the scattered field fairly well.

From Figures 4 and 5 we see that there is good agreement between the scattered signal with the scattering cancellation obtained from HFSS, CST, and the CAD (theoretical) method. We also see that the scattered signal is greatly reduced deep inside the pulse, but much less so near the edges of the pulse. This is because deep inside the pulse, the signal behaves more like a pure sinusoid at the carrier frequency, and the scattering cancellation scheme is designed to eliminate the scattered signal at the carrier frequency. Overall, the cancellation of scattering is achieved to a good extent, so that the total energy in the scattered signal is greatly diminished through the active cancellation (this will be quantified in section 5.4).

Spectrograms (short-time Fourier transforms) of the incident radar signal and the scattered signal from the plate with scattering cancellation are given in Figures 6 and 7, respectively.

The spectrogram of the scattered signal with the scattering cancellation active (shown in Figure 7), when compared to the spectrogram of the incident signal (shown in Figure 6), shows that the cancellation of

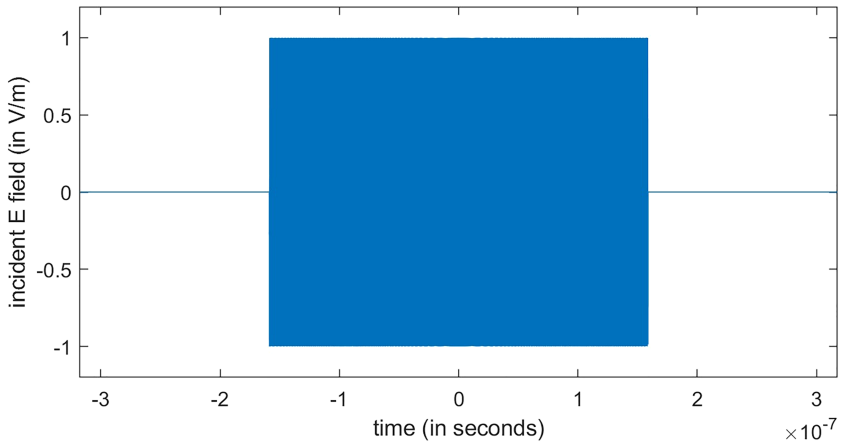

Figure 9. The incident rectangular chirped pulse signal.

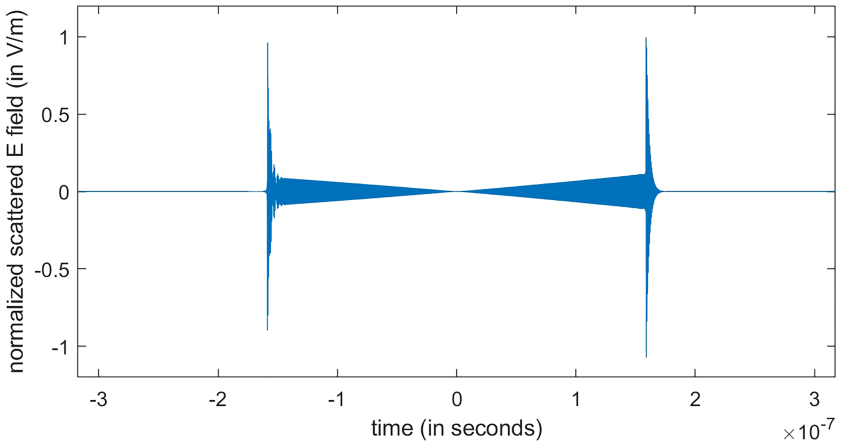

Figure 10. The scattered signal from the rectangular chirped pulse incident signal with scattering cancellation from the CAD method for no delay in the circuit, $Q = 10$.

the carrier frequency and all other frequencies is well achieved in the middle of the pulse, but toward the pulse edges the cancellation is not complete. This is consistent with the results shown in Figures 4 and 5.

From another point of view, the system must obey causality. When the incident signal first impinges on the object (plate), the patch has not yet started to radiate. It takes some time for the information to travel from the sensor through the electronics to the patch. Hence, there has to be a time interval after the signal first hits the system when the cancellation of the scattered signal is not good, and we are in effect seeing only the natural scattering of the object (plate). This is why the scattered signal is strong at the left edge of the pulse in Figure 4. Similarly, the scattered signal is strong at the right edge of the pulse because it takes time for the information that the signal has been switched off to travel through the system.

5.2. Gaussian Pulse Modulated Radar Signal

The system of plate, patch, and sensor, along with the amplifier and phase shifter circuit analyzed in section 3, is again considered here. The signal transmitted from the radar is now taken to be a Gaussian pulse modulated signal of carrier frequency 1.575 GHz, and the width of the pulse (based on the time constant of the envelope) is 200 ns. In Figure 8 the signal scattered from the plate without scattering cancellation, as well as the normalized scattered signal from the plate with the scattering cancellation (implemented with the patch and sensor on it), is shown, with the coefficients computed using Ansys HFSS. When we compare this

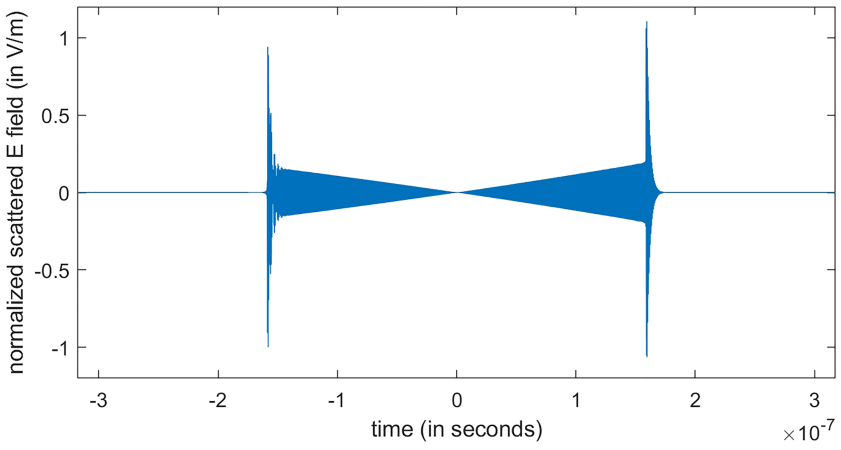

Figure 11. The scattered signal from the rectangular chirped pulse incident signal with scattering cancellation from the CAD method for a one-wavelength delay in the circuit, $Q = 10$.

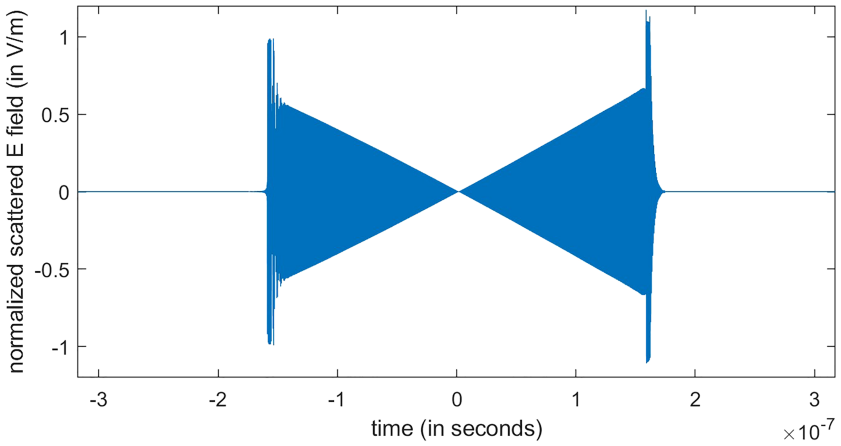

Figure 12. The scattered signal from the rectangular chirped pulse incident signal with scattering cancellation from the CAD method for a five-wavelength delay in the circuit, $Q = 10$.

with the scattering cancellation achieved with the rectangular pulse modulated signal in section 4, it is clear that the scattering cancellation is better for the signal with the Gaussian pulse envelope. This is because the Gaussian pulse envelope has a narrower bandwidth than the rectangular pulse envelope. In general, the extent of the scattering cancellation depends on the bandwidth of the radar signal, as well as the bandwidth of the system, including the patch, the sensor, and the amplifier and phase shifter circuit.

5.3. Rectangular Pulse Chirped Radar Signal

Here the system is once again the same as used in the previous two sections. We continue to examine the case of the rectangular plate with a patch antenna and a sensor connected through an amplifier and phase shifter circuit as described previously in section 2. For the rectangular pulse modulated signal the patch antenna with a quality factor of 58.24 was adequate to achieve a significant RCS reduction, but since the rectangular chirped pulse signal used in this section has a much greater bandwidth, the bandwidth of the patch had to be increased in order to achieve a good RCS reduction. Therefore, we assume a patch antenna with quality factor of 10 to cancel the scattering of a rectangular chirped pulse having a 2% variation in frequency along the width of the pulse, with a center frequency of 1.575 GHz. (The frequency starts at a beginning frequency that is 1% lower than 1.575 GHz at the beginning of the pulse, and linearly increases to a frequency that is 1% higher than 1.575 GHz at the end of the pulse.) The incident radar signal at the surface of the plate is shown in Figure 9, which is a rectangular chirped pulse of width 317.46 ns.

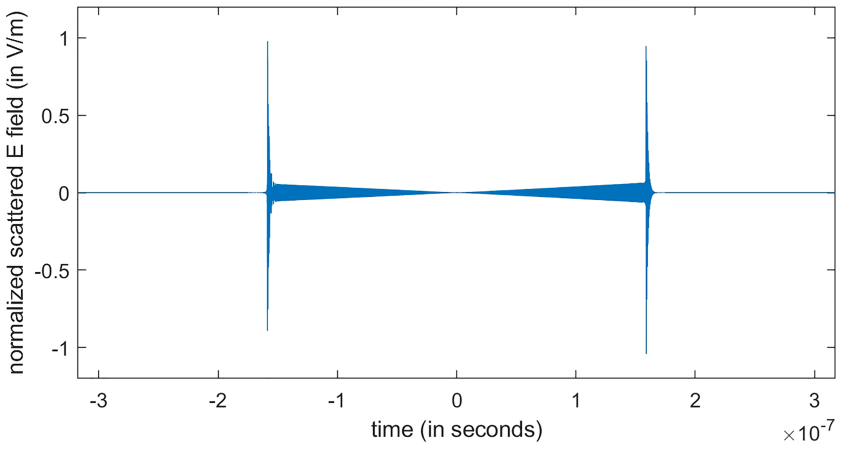

Figure 13. The scattered signal from the rectangular chirped pulse incident signal with scattering cancellation from the CAD method for no delay in the circuit, $Q = 5$.

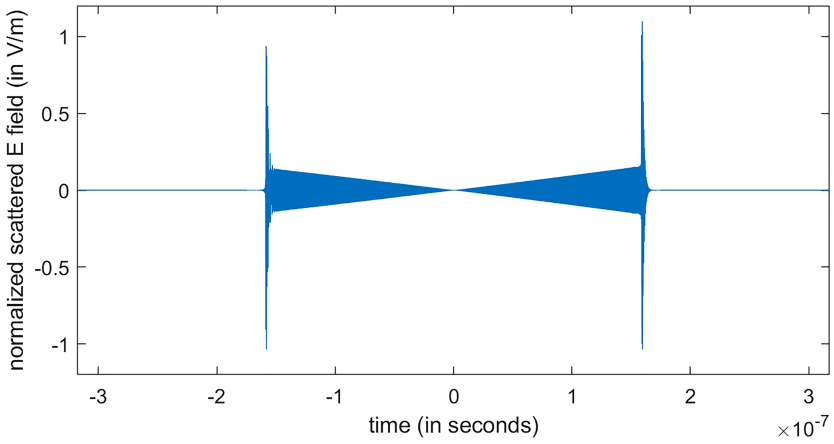

Figure 14. The scattered signal from the rectangular chirped pulse incident signal with scattering cancellation from the CAD method for a *one*-wavelength delay in the circuit, $Q = 5$.

The normalized scattered signal from the plate with the scattering cancellation, implemented with the patch and sensor on it, is given in Figure 10 for the case with no delay in the system. This result is calculated using the CAD formula based on the theoretical analysis described in section 4.

In this case and all the previous cases, we have assumed that there is no time delay in the signal propagating through the circuit between the sensor and the patch. However, the effect of delay in the circuit can greatly impact the effectiveness of the scattering cancellation. This can be seen in the normalized scattered signal with scattering cancellation calculated assuming a delay in the circuit that is chosen as one guided wavelength and five guided wavelengths, in Figures 11 and 12, respectively. The delay of one wavelength and five wavelengths (with wavelength meaning the guided wavelength λ_g) corresponds to 0.635 and 3.175 ns of time delay, respectively, at the carrier frequency of 1.575 GHz, assuming $\varepsilon_r^{eff} = 1.885$ (corresponding to a dispersionless transmission line with a substrate relative permittivity of $\varepsilon_r = 2.2$). Once again, the scattered signal has been calculated using the theoretical analysis described in section 4. In equation (23) we now use a value of physical delay L that is chosen to be

$$(\omega_0/c)\sqrt{\varepsilon_r^{eff}}L = 2\pi \text{ or } 5(2\pi). \tag{32}$$

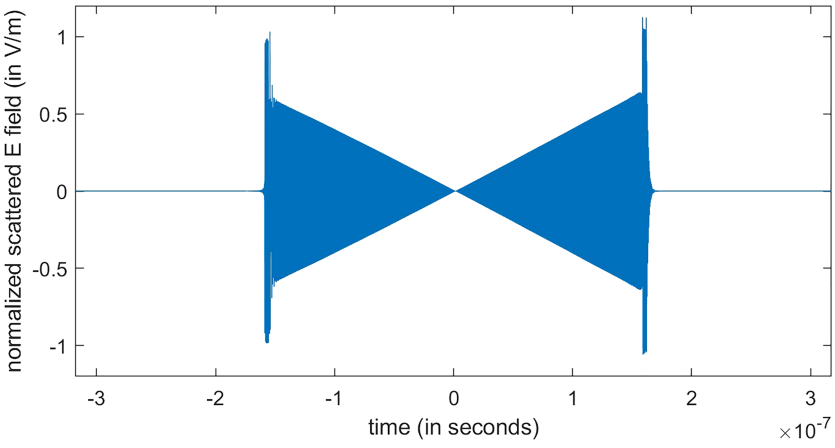

Figure 15. The scattered signal from the rectangular chirped pulse incident signal with scattering cancellation from the CAD method for a *five*-wavelength delay in the circuit, $Q = 5$.

Table 1
The Figure of Merit (FOM) for a Chirped Pulse

Q/Delay	0	0.25 λ_g	0.5 λ_g	1 λ_g	2 λ_g	5 λ_g	10 λ_g
$Q = 5$	0.59%	0.73%	0.91%	1.5%	3.3%	14.3%	48.0%
$Q = 10$	1.1%	1.2%	1.4%	2.0%	3.9%	15.1%	49.3%
$Q = 20$	2.5%	2.7%	2.9%	3.6%	5.6%	17.4%	52.8%
$Q = 50$	12.6%	13.0%	13.4%	14.4%	17.3%	32.4%	74.7%
Q = 100	91.1%	92.9%	94.7%	98.7%	107.8%	142.6%	211.6%

From Figures 11 and 12 it becomes evident that when there is a large amount of time delay in the circuit, it can greatly reduce the effectiveness of the scattering cancellation.

The bandwidth of the patch is then further increased by setting $Q = 5$, and for the same rectangular chirped pulse the scattered radar signal for delays of 0, 1, and 5 wavelengths are given in Figures 13–15, respectively, which show a slightly greater reduction in RCS compared to the cases for $Q = 10$.

5.4. FOM

In order to quantify the extent of the RCS reduction achieved by the proposed method, a figure of merit (FOM) is defined as a useful metric based on the energy in the scattered signal. The FOM is defined as the ratio of the energy in the scattered signal when the proposed RCS reduction scheme is active, to the energy in the scattered signal from the same object without any RCS reduction (no patch antenna present). Here we study the effects of delay in the system and the bandwidth of the antenna, based on the FOM. Results are presented in Tables 1 and 2. Table 1 shows results for a rectangular modulated chirped pulse, for the same chirped pulse used in section 5.3 (a 2% frequency variation over the pulse width, a carrier frequency 1.575 GHz, and a pulse width of 317.46 ns). Table 2 shows results for the rectangular modulated pulse with the same pulse width (a sinusoidal carrier of frequency 1.575 GHz modulated by a rectangular pulse of width 317.46 ns).

The FOM values for the chirped rectangular pulse are given in Table 1 for different delays in the system and different Q values (impedance bandwidths) for the patch antenna. From Table 1 we can observe that in order to get a good RCS reduction (small FoM), the bandwidth of the patch must be at least as large as that of the signal. For no delay in the system, the RCS reduction consistently gets smaller as the patch bandwidth increases. For a given delay, the amount of RCS reduction "saturates" as the patch bandwidth increases, with the limiting (minimum) value of the FoM that is achievable depending on the delay. The larger the delay is, the larger is the minimum FoM that can be achieved.

For a given patch bandwidth, Table 1 shows that the RCS reduction consistently gets worse as the delay in the system increases. It probably approaches something around 200% in the extreme limit. (This is a speculation based on physical reasoning; it cannot be verified from Table 1 since the maximum delay in the table is 10 wavelengths, and the FOM has not reached a limiting value yet in most cases.) This is because the patch is still radiating a counter (canceling) signal that is similar in amplitude to the signal that is scattered by the object (plate) itself, but the counter signal is now completely separate from the scattered signal by the object itself due to the large delay, giving us essentially two similar scattered signals where there would have originally been only one without the RCS reduction scheme. This means that the scattered signal will now have approximately twice the energy as would the scattered signal from the object itself.

The FOM values for the rectangular modulated pulse are given in Table 2 for various delays in the system, using the same patch antenna in section 5.1 (having a Q of 58.24). For this pulse the bandwidth of the pulse is quite small (about 0.3%), so even this narrowband patch that has a bandwidth of about 1.2% is successful at greatly lowering the RCS.

6. Sensor Design

The basic sensor described before is a bent monopole with two orthogonal horizontal branches in the form of microstrip lines on the surface of the dielectric. The sensor is fed by a coaxial probe that connects to the point where the two branches of microstrip line join. The two orthogonal lines are meant to pick up orthogonal polarizations of the incident field from the radar (although the incident field is purely x directed in the examples here).

This sensor is affected by the mutual coupling from the patch. It therefore should ideally be placed at a location where the coupling from the patch is small, to keep the design as simple as possible. In order to

Table 2
The Figure of Merit (FOM) for a Rectangular Modulated Pulse

Q/Delay	0	0.25 λ_g	0.5 λ_g	1 λ_g	2 λ_g	5 λ_g	10 λ_g
$Q = 58.24$	2.0%	2.05%	2.1%	2.0 %	2.4%	3.0%	4.0%

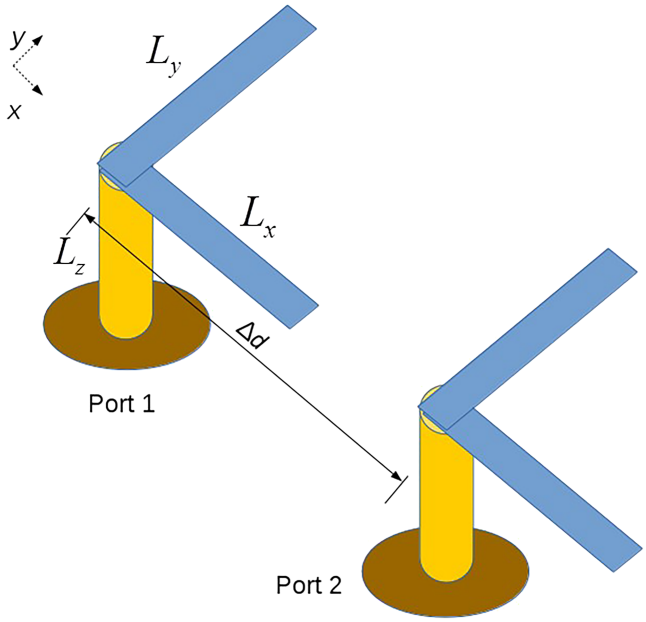

Figure 16. The design of the supersensor, which consists of two identical regular sensors.

remove the effect of mutual coupling to the sensor from the patch antenna, a "supersensor" design is introduced, which consists of two identical regular sensors described above, placed close to each other along the surface of the object (plate) as shown in Figure 16. The separation between the two individual sensors in the "supersensor" design is taken to be 95 mm (which is half a wavelength at the carrier frequency of 1.575 GHz). The outputs of both sensors are multiplied by complex weights and added together so that the signals picked up from mutual coupling from the patch cancel each other, but the signals from the incident signal do not cancel.

The supersensor is then able to detect the incident wave from the radar, but in the absence of the incident wave, when the nearby defending patch antenna is excited, the supersensor has negligible output. In other words, the supersensor does not detect the direct radiation from the patch antenna. Figure 17 shows the signal scattered from the plate without scattering cancellation, as well as the normalized scattered signal from the plate with the scattering cancellation, which is implemented with the patch and the supersensor on it and is computed using the CST Microwave Studio transient solver.

Figures 17 and 4 have the same incident radar signal, which is a rectangular pulse modulated signal of carrier frequency 1.575 GHz and a pulse width of 200 ns. Comparison of Figures 4 and 17 shows that the scattered signal from the plate (with the patch and the sensor) is the same whether we use the regular sensor or the supersensor. The advantage of the supersensor, however, is that the output of the supersensor is not affected by the mutual coupling with the patch and therefore the supersensor can be placed close to the patch, for example, a quarter wavelength away, without having to account for mutual coupling in the design.

In order to see how the supersensor compares with the regular sensor, the supersensor and the regular sensor were both placed at a distance of one-half of a free-space wavelength from the patch (measured from the closest patch edge) in the H plane direction, in two separate simulations. The weights applied to the output of the two individual sensors in the supersensor to give the total output voltage in this case are given by 1 and 0.7454 ∠230°. The supersensor can be placed at any distance close to the patch, but the weights would

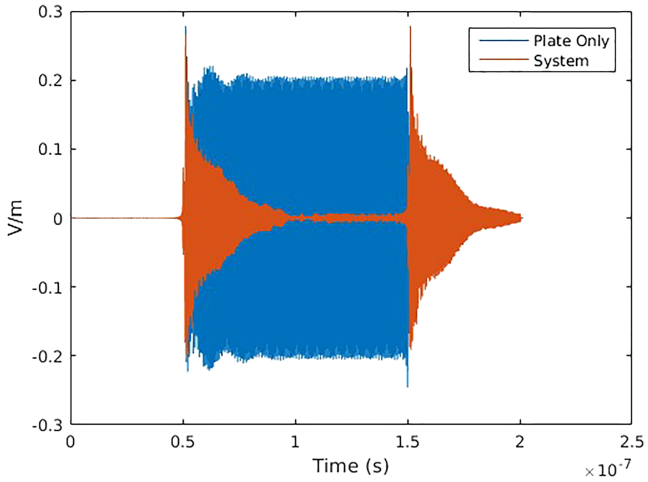

Figure 17. The scattered signal from the rectangular pulse modulated incident signal, without scattering cancellation (blue curve) and also with scattering cancellation (red curve), from the CST transient solver. A supersensor is used instead of a regular sensor.

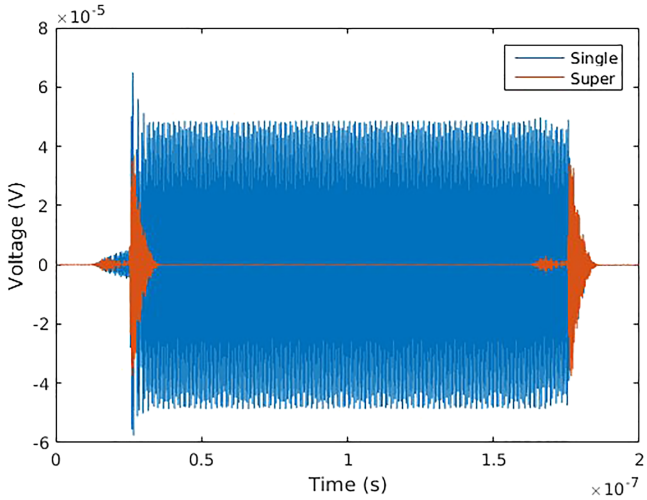

Figure 18. Open-circuit voltage at the output of the sensors due to only the patch radiation for a $\lambda_0/2$ separation from the patch. Results are shown for a single sensor (blue curve) and a supersensor (red curve).

depend on the location relative to the patch to avoid mutual coupling from the patch. A full-wave simulation of the patch and supersensor when the patch is excited at the carrier frequency is done to determine the open-circuit output voltages at the two ports of the supersensor, and the weights are then determined so that the weighted sum is zero for a sinusoidal excitation of the patch.

The output of the supersensor and the regular (single) sensor due to only the patch radiation are compared in Figure 18. The patch radiates the same transient signal that is used to minimize the RCS from the plate when the incident signal is the rectangular modulated pulse, as discussed previously. Figure 18 shows that the supersensor receives much less of an output voltage than does the regular sensor.

The output of the supersensor and the regular (single) sensor due to the incident signal, including the feedback (mutual coupling) effect of the patch is then compared in Figure 19. Figures 18 and 19 show that while the patch radiation has almost no impact on the output of the supersensor, the supersensor is still able to detect the incident radar signal well. Figure 19 shows that the regular sensor produces an output voltage that is about 25% higher than from the supersensor. This difference is due to the

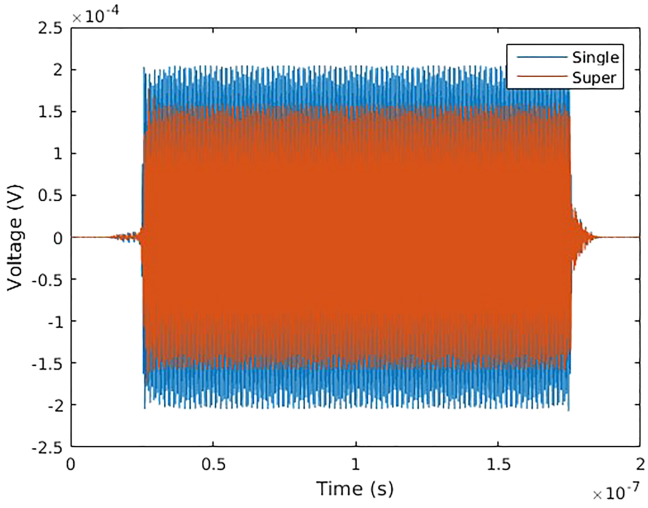

Figure 19. Open-circuit voltage at the sensors due to incident radar signal in the presence of the patch for $\lambda_0/2$ separation from the patch.

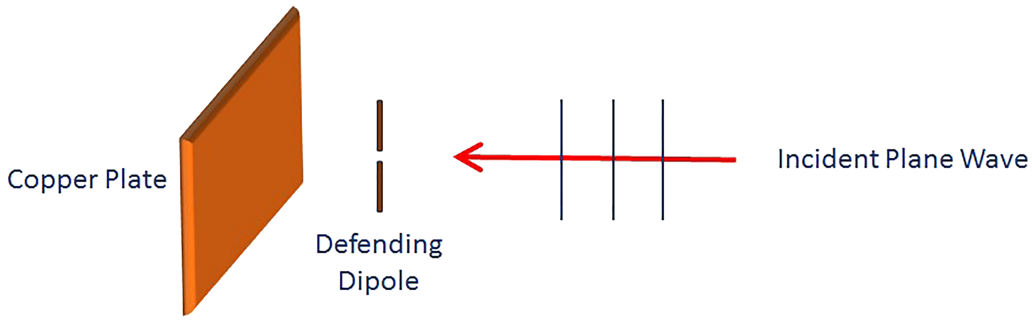

Figure 20. The setup for studying how the angular range of the scattering cancellation varies with the size of the object (plate), which is defended from the radar signal by a dipole antenna.

mutual coupling with the patch which, though fairly small, is not negligible for the regular sensor. In the RCS reduction scheme, the amplifier coefficient $A(\omega_0)$ compensates for the mutual coupling, as seen in equations (15) and (12). However, if the supersensor is used, the design becomes slightly simpler since $F(\omega) \approx 0$ and thus $B(\omega) \approx B_0(\omega)$.

7. Variation of the Angular Area of Scattering Cancellation With Size and Shape of the Object

In order to successfully avoid detection by a radar it is desirable to achieve scattering cancellation over a large region of space in the far-field region of the object, where the radar is located. It has been found that in the far-field region the angular region/area over which scattering cancellation is achieved varies with the size of the object. For the purpose of investigating how the size of an object can affect the angular region over which sufficient scattering cancellation can be achieved, we use the canonical problem shown in Figure 20. It consists of a square copper plate on which the signal from the radar at a single frequency of 5.5 GHz is normally incident. The plate is defended from the radar by a resonant length dipole antenna placed a quarter wavelength in front of the plate. The dipole is excited with an amplitude and phase to provide maximum scattering cancellation at broadside. Although a dipole is placed a quarter of a wavelength away from the object (plate) instead of using a microstrip antenna placed on the surface of the object, and the frequency is different from the previous cases, the physical principle of the RCS cancellation is very similar in both cases.

The plate size is varied and the angular region of scattering cancellation is defined as the angular area in the far-field region where the energy in the scattered signal has been reduced by 20 dB over the maximum field strength at broadside without the scattering cancellation. The angle of the region over which scattering cancellation is achieved for plates of varying sizes is found by simulation in HFSS and given in Table 3. The angle of scattering cancellation has also been calculated through theoretical analysis based on physical optics, which leads to the approximate CAD formula

$$\phi_{\max} = \frac{2}{k_0 L}(0.7887), \tag{33}$$

where L is the length (width) of the square plate and k_0 is the wavenumber of free space. The calculated angle of scattering cancellation from the CAD formula (33) for different sizes of the plate is also included in Table 3.

Table 3
The Angle of Scattering Cancellation Versus Size of Plates

Size of the plate (mm)	Angle of scattering cancellation from HFSS (degrees)	Angle of scattering cancellation from CAD formula (degrees)
500 × 500	3.16	3.14
400 × 400	3.87	3.92
300 × 300	5.00	5.22
200 × 200	7.91	7.84
100 × 100	14.39	15.68

The angular range of scattering cancellation also depends on the curvature of the object and has been examined by comparing the angular region of scattering cancellation in the far-field (the region where the energy in the signal has been reduced by 20 dB over the maximum field strength at broadside without scattering cancellation) for a square plate and a cylinder of comparable sizes. For this comparison the angle of scattering

Table 4
The Angle of Scattering Cancellation for a Plate and a Cylinder of Comparable Size

Structure (plate or cylinder)	Angle of scattering cancellation from HFSS (degrees)
Plate of size 200 mm × 200 mm	7.91
Cylinder of diameter 200 mm	13.77

cancelation for a square plate of side length 200 mm and that for a cylinder of diameter 200 mm and infinite height are found by simulation in HFSS and given in Table 4.

From the results presented in Tables 3 and 4, it is evident that the angle of scattering cancellation decreases as the size of the object is increased, and the angle of scattering cancellation is also greater for a curved object as compared to an object with a flat surface.

8. Conclusions

In this paper we have explored the feasibility of reducing the monostatic RCS of an object in a certain direction by placing a sensor and a radiating patch antenna element on the surface of the object, connected together by an amplifier, phase shifter, and transmission line. The analysis suggests that the proposed RCS reduction scheme will perform best in a low frequency regime, whereby properly optimizing the system enables a partial cancellation of a scattered radar signal waveform of arbitrary shape, for example, one having rectangular or Gaussian envelope, or a chirped pulse, as long as the bandwidth of the signal is within the bandwidth of the antenna and associated electronics. The delay in the system due to the transmission line and associated electronics is a major limitation of the RCS reduction. A FOM based on the energy in the scattered signal has been used to quantify the amount of RCS reduction achievable using the proposed scheme. A larger RCS reduction is achievable by using a patch antenna with a larger bandwidth and by minimizing the delay in the system. In such cases the energy in the scattered signal can be reduced to less than one percent of the energy that the scattered signal would have had without the RCS reduction scheme. The angular region over which the scattering cancellation is achieved decreases as the size of the object increases, and is greater for objects with curved surfaces (such as a cylinder) as opposed to objects with plane surfaces (such as a plate). Possible applications include interference control for known EM radiating sources (e.g., minimizing interference from wind farm scattering in friendly radar systems). Extensions include using multiple antennas and multiple sensors to achieve RCS reduction at multiple angles or for wider angles.

Acknowledgments
This research has been supported in part by the Air Force Office of Scientific Research under Award FA9550-13-1-0078, a GEAR grant from the University of Houston, and the Army Research Office under Award W911NF-17-1-0478. Data archiving for this project has been done with the 4TU.ResearchData repository (https://researchdata.4tu.nl/en/home/). Name of the data set is "RCS Reduction using Anennas and Sensors"; DOI of the data set is 10.4121/uuid:084de133-4aa9-441f-a488-5995ee786bdb; http://doi.org/10.4121/uuid:084de133-4aa9-441f-a488-5995ee786bdb is the URL of the data set.

References

Albanese, R., & Onofrei, D. (2017). On the active manipulation of EM fields in open waveguides. *Wave Motion*, *69*, 91–107.
Albanese, R., & Onofrei, D. (2016). Control of electromagnetic fields, Air Force Office of Scientific Research YIP award number FA9550-13-1-0078.
Balanis, C. A. (2012). *Advanced engineering electromagnetics* (2nd ed.). New Jersey: John Wiley and Sons.
Baskey, H. B., Johari, E., & Akhtar, M. J. (2017). Metamaterial structure integrated with a dielectric absorber for wideband reduction of antennas radar cross section. *IEEE Transactions on Electromagnetic Compatibility*, *59*(4), 1060–1069.
Brock, B. C., et al. (2012). Radar cross-section reduction of wind turbines (Part 1), Sandia Report SAND2012-0480.
Chen, P.-Y., Argyropoulos, C., & Alu, A. (2013). Broadening the cloaking bandwidth with non-Foster metasurfaces. *Physics Review Letters*, *111*(23).
Du, J., Liu, S., & Lin, Z. (2012). Broadband optical cloak and illusion created by the low order active sources. *Optics Express*, *20*(8), 8608–8617.
Ghayekhloo, A., Abdolali, A., & Mohseni Armaki, S. H. (2017). Observation of radar cross-section reduction using low-pressure plasma-arrayed coating structure. *IEEE Transactions on Antennas and Propagation*, *65*(6), 3058–3064.
Guevara Vasquez, F., Milton, G. W., & Onofrei, D. (2009a). Active exterior cloaking for 2D Laplace and Helmholtz equations. *Physics Review Letters*, *103*(7).
Guevara Vasquez, F., Milton, G. W., & Onofrei, D. (2009b). Broadband exterior cloaking. *Optics Express*, *17*(17), 14,800–14,805.
Guevara Vasquez, F., Milton, G. W., & Onofrei, D. (2011). Exterior cloaking with active sources in two dimensional acoustics. *Wave Motion*, *48*(6), 515–524.
Guevara Vasquez, F., Milton, G. W., & Onofrei, D. (2012). Mathematical analysis of the active exterior cloak for 2D quasistatic electromagnetics. *Analysis and Mathematical Physics*, *2*(3), 231–246.
Guevara Vasquez, F., Milton, G. W., Onofrei, D., & Seppecher, P. (2011). Transformation elastodynamics and active exterior acoustic cloaking, Acoustic metamaterials: Negative refraction, imaging, lensing and cloaking. *arXiv*, *1105*, 1221.
Haji-Ahmadi, M.-J., Nayyeri, V., Soleimani, M., & Ramahi, O. M. (2017). Pixelated checkerboard metasurface for ultra-wideband radar cross section reduction. *Scientific Reports*, *7*.
Harrington, R. F. (2001). *Time-harmonic electromagnetic fields*. New York, NY: John Wiley and Sons/IEEE Press.
Hubenthal, M., & Onofrei, D. (2016). Sensitivity analysis for the active control of the Helmholtz equation. *Applied Numerical Mathematics*, *106*, 1–23.
Jackson, D. R. (2019). In J. Volakis (Ed.), *Microstrip antennas, Chapter 7 in Handbook of Antenna Engineering* (5th ed.). New York, NY: McGraw-Hill.
Kord, A., Sounas, D. L., & Alù, A. (2016). *Ultrathin active cloak with balanced loss and gain, 2016 IEEE International Symposium on Antennas and Propagation* (pp. 369–370). Puerto Rico: Fajardo.
Li, H., Zhang, L., Song, Z., & Zeng, X. (2016). *RCS reduction of active periodical structural scatterer, 2016 11th International Symposium on Antennas, Propagation and EM Theory (ISAPE)* (pp. 303–306). Guilin: IEEE.

Li, K., Liu, Y., Jia, Y. O., & Guo, Y. J. (2017). A circularly polarized high-gain antenna with low RCS over a wideband using chessboard polarization conversion metasurfaces. *IEEE Transactions on Antennas and Propagation*, *65*(8), 4288–4292.
Ma, Q., Mei, Z. L., Zhu, S. K., & Jin, T. Y. (2013). Experiments on active cloaking and illusion for Laplace equation. *Physics Review Letter*, *111*(17).
Miller, D. A. B. (2006). On perfect cloaking. *Optics Express*, *14*(24), 12457–12466.
Naqvi, A., & Ling, H. (2013). A study of radar feature of wing turbines in the HY band. *Progress In Electromagnetics Research*, *143*, 605–621.
Norris, A. N., Amirkulova, F. A., & Parnell, W. J. (2012). Source amplitudes for active exterior cloaking. *Inverse Problems*, *28*(10).
Onofrei, D. (2012). On the active manipulation of fields and applications. The quasistatic case. *Inverse Problems*, *28*(10).
Onofrei, D. (2014). Active manipulation of fields modeled by the Helmholtz equation. *Journal of Integral Equations and Applications*, *26*(4).
Palmer, R. D., & Torres, S. (2011). *Advanced detection and mitigation of wind turbine clutter for the multi-mission phased array radar (MPAR) program*. Atmospheric Radar Research Center: University of Oklahoma.
Pinto, J., Matthews, J. C. G., & Sarno, G. C. (2010). Stealth technology for wind turbines. *IET Radar Sonar Navigation*, *4*(1), 126–133.
Raza, M. B., & Fickenscher, T. H. (2013). Investigating the radar returns of a wind turbine, PIERS Proceedings, pp. 730-733, Taipei.
Selvanayagam, M., & Eleftheriades, G. V. (2012). An active electromagnetic cloak using the equivalence principle. *IEEE Antennas and Wireless Propagation Letters*, *11*, 1226–1229.
Selvanayagam, M., & Eleftheriades, G. V. (2013). Experimental demonstration of active electromagnetic cloaking. *Physics Review X*, *3*(4).
Semenikhin, A. I., & Chernokolpakov, A. I. (2017). *Active cancellation of radar cross section of large aircraft using conformal 2-port magnetic T-shaped antenna, 2017 Radiation and Scattering of Electromagnetic Waves (RSEMW) conference*. Russia: Divnomorskoe.
Semenikhin, A. I., & Chernokolpakov, A. I. (2019). *Active cancellation of the RCS of a large aircraft using of stealth 4-Port magnetic antenna with heterogenic ferrite core, 2019 IEEE Conference of Russian Young Researchers in Electrical and Electronic Engineering (EIConRus)*. Russia: Saint Petersburg and Moscow.
Sengupta, S., Jackson, D. R.,Onofrei, D., & Council, H. (2017). Reduction of radar cross section using active microstrip antenna elements, 2017 IEEE Antennas and Propagation Society International Symposium.
Sheng, X., & Yuanming, X. (2012). *Assemble an active cancellation stealth system*. Defense: Electronics.
Sheng, X., & Yuanming, X. (2014a). Simulation analysis of an active cancellation stealth system. *Optik*, *125*(18).
Sheng, X., & Yuanming, X. (2014b). Research on active cancellation stealth technique. *Optik*, *125*(20).
Singh, H., & Jha, R. M. (2015). *Active radar cross section reduction: Theory and application* (1st ed.). Delhi, India: Cambridge University Press.
Soric, J. C., Chen, P. Y., Kerkhoff, A., Rainwater, D., Melin, K., & Alu, A. (2013). Demonstration of an ultralow profile cloak for scattering suppression of a finite-length rod in free space. *New Journal of Physics*, *15*(3), 033037.
Su, J., Kong, C., Li, Z., Yin, H., & Yang, Y. (2017). Wideband diffuse scattering and RCS reduction of microstrip antenna array based on coding metasurface. *Electronics Letters*, *53*(16), 1088–1089.
Su, J., Kong, C., Li, Z., Yuan, X., & Yang, Y. (2017). Ultra-wideband and polarization-insensitive RCS reduction of microstrip antenna using polarization conversion metasurface. *Applied Computational Electromagnetics Society Journal*, *32*(6), 524–530.
Sui, Y., Gu, >H., & Yang, C. (2017). Reconfigurable stealth radome using active frequency selective surface technology, 2017 IEEE International Conference on Computational Electromagnetics (ICCEM), pp. 273-275, Kumamoto.
Tennant, A., & Chambers, B. (2005). RCS reduction of spiral patch antenna using a PSS boundary, IEE Proceedings-Radar. *Sonar and Navigation*, *152*(4), 248–252.
Ufimtsev, P. Y. (1996). Comments on diffraction principles and limitations of RCS reduction techniques. *Proceedings of the IEEE*, *84*(12), 1830–1851.
Xu, L., Feng, D., Liu, Y., Pan, X., & Wang, X. (2015). A three-stage active cancellation method against synthetic aperture radar. *IEEE Sensors Journal*, *15*(11), 6173–6178.
Zhang, L., Wan, X., Liu, S., Yin, J. Y., Zhang, Q., Wu, H. T., & Cui, T. J. (2017). Realization of low scattering for a high-gain Fabry-Pérot antenna using coding metasurface. *IEEE Transactions on Antennas and Propagation*, *65*(7), 3374–3383.
Zheng, H. H., Xiao, J. J., Lai, Y., & Chan, C. T. (2010). Exterior optical cloaking and illusions by using active sources: A boundary element perspective. *Physics Review B*, *81*(19).
Zheng, Y.-J., Gao, J., Zhou, Y.-L., Cao, X.-Y., Xu, L.-M., Li, S.-J., & Yang, H.-H. (2017). Metamaterial-based patch antenna with wideband RCS reduction and gain enhancement using improved loading method. *IET Microwaves Antennas and Propagation*, *11*(9), 1183–1189.